REVIEW ARTICLE   OPEN

The resurrection of tellurium as an elemental two-dimensional semiconductor

Gang Qiu[1,2], Adam Charnas [1,2], Chang Niu [1,2], Yixiu Wang[3], Wenzhuo Wu[3] and Peide D. Ye [1,2 ✉]

The graphene boom has triggered a widespread search for novel elemental van der Waals materials thanks to their simplicity for theoretical modeling and easy access for material growth. Group VI element tellurium is an unintentionally p-type doped narrow bandgap semiconductor featuring a one-dimensional chiral atomic structure which holds great promise for next-generation electronic, optoelectronic, and piezoelectric applications. In this paper, we first review recent progress in synthesizing atomically thin Te two-dimensional (2D) films and one-dimensional (1D) nanowires. Its applications in field-effect transistors and potential for building ultra-scaled Complementary metal–oxide–semiconductor (CMOS) circuits are discussed. We will also overview the recent study on its quantum transport in the 2D limit and progress in exploring its topological features and chiral-related physics. We envision that the breakthrough in obtaining high-quality 2D Te films will inspire a revisit of the fundamental properties of this long-forgotten material in the near future.

INTRODUCTION

Since the debut of Moore's Law in 1965, the cadence of semiconductor manufacturing has been governed by this empirical observation. It is evident that the downsizing trend of transistors cannot be sustained forever. The latest generations of CMOS devices have had to overcome some serious challenges in power dissipation, reliability, and mobility degradation, for example. As leading industry goliaths are devoting themselves to developing 3-nm and 2-nm silicon-based technology nodes, hopes have also been cast onto 2D material platforms as an alternative solution to extend the long-living Moore's Law. 2D materials generally feature interlayer van der Waals (vdW) forces between atomic sheets of covalently bonded atoms. As a rule of thumb, to design field-effect transistors (FETs) with sufficient electrostatic control, the channel thickness should be no more than one-third of the gate length. For example, in a transistor with a gate length of 3 nm, the channel has to be as thin as 1 nm, i.e., 2–3 layers of atoms. In an ultra-thin body (UTB) film made from conventional 3D bulk material, surface scattering and unsaturated dangling bonds will deteriorate the carrier mobility and device performance. Whereas in vdW materials, the interlayer vdW bonds allow easy cleavage into a perfect dangling-bond-free surface and sustain reasonably high mobility even in the monolayer regime[1]. Additionally, there is a large catalog of 2D materials that covers a wide electronic spectrum from metals to semiconductors to insulators, which offers the potential to build all-2D-material circuits by stacking different 2D materials like Lego[2,3].

Beyond promising electronic applications, 2D material systems are also ideal testbeds to explore exotic transport properties in the 2D limit from a condensed-matter physics perspective. For instance, exfoliated 2D films offer a fast and simple approach towards high-quality 2D electron gases (2DEGs) without requiring the sophisticated growth of hetero-structures in conventional 2DEGs[4]. For example, the quantum Hall effect was achieved in monolayer graphene[5–7], which spurred advancements in manipulating topological states and correlated states in graphene

systems[8–11]. Additionally, many other bizarre physical phenomena that are only exhibited in 2D systems were found in 2D materials such as the quantum spin Hall effect[12] and quantum anomalous Hall effect[13,14].

Among the vast collection of 2D materials[15], single elemental materials are exceptionally attractive thanks to their simplicity for theoretical modeling and material growth. However, only a few elemental 2D materials with energetically stable phases have been identified and experimentally demonstrated, *e.g.* graphene[16], phosphorene[17,18], germanene[19,20], silicene[21], stanene[22,23], and bismuthene[24]. The suffix "*-ene*" was initially used in graphene to emphasize the π-bonds formed in unsaturated carbon atoms. Later the nomenclature was extended to other elemental 2D materials to refer to their monolayer form as an analogy to graphene. A new member of elemental 2D materials, monolayer tellurium (dubbed as "tellurene") was first introduced in 2017. Several stable tellurene allotropes in the few-layer or monolayer limit, including 1T-MoS$_2$-like (α-Te), metastable tetragonal (β-Te), and 2H-MoS$_2$-like (γ-Te) structures were first predicted by Z. Zhu et al.[25] and others[26–29] through ab initio simulations. Subsequently, the β-Te phase was experimentally demonstrated by epitaxially deposited tellurene islands on graphite substrates and confirmed via scanning tunneling microscopy[25,30]. In 2018, by reducing bulk trigonal tellurium to mono-layers, trigonal tellurene was theoretically proposed[27] and experimentally demonstrated in different material synthesis techniques including CVD[31], hydro-thermal growth[32], and molecular beam epitaxy (MBE)[33]. The 1D van der Waals properties of 2D tellurene films grown by the hydrothermal method were even reported earlier in 2017[33]. In the literature, the term *tellurene* is broadly used for all 2D allotropes that consists of only tellurium atoms. Yet among all the tellurene allotropes, trigonal tellurene is the most well-established form, since it inherits its bulk crystal structure and physical properties to a large extent. Experimental progress has also been predominantly focused on trigonal tellurene, due to its relatively mature production via the hydrothermal method as well as its stability in

[1]Elmore Family School of Electrical and Computer Engineering, Purdue University, West Lafayette, IN 47907, USA. [2]Birck Nanotechnology Center, Purdue University, West Lafayette, IN 47907, USA. [3]School of Industrial Engineering, Purdue University, West Lafayette, IN 47907, USA. ✉email: yep@purdue.edu
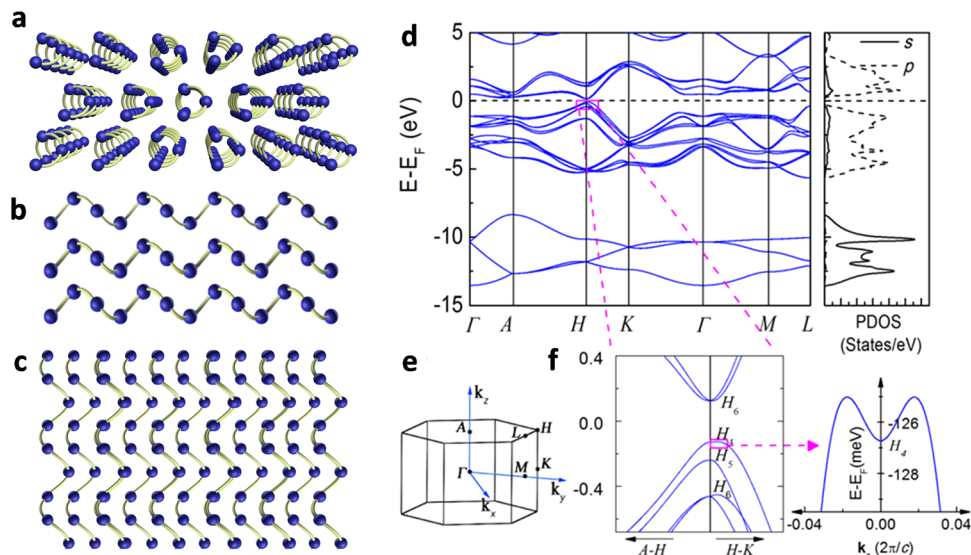
Fig. 1 **Crystal structure and band structure of 2D tellurium. a** The trigonal Te crystal structure consists of spiral chains with three-fold screw symmetry held together by inter-chain van der Waals bonds. The atomic chains can be arranged into 2D films. **b** Side view and (**c**) top view of 2D Te films. **d** Calculated band structure of Te including SOC and corresponding partial density of states (PDOS) with contributions from 5s- and 5p-orbital electrons. **e** First Brillouin zone of Te. **f** Left panel: Zoomed-in band features near the direct band edge at the H point. Right panel: Camel back humps in the vicinity of the valence band edge. **d–f** are reproduced from ref. [88].

air[32]. Therefore, we will primarily focus on trigonal tellurene for the rest of this paper.

Te is a group VI chalcogen that was first discovered in the late 18th century and was named after the Latin word, *tellus*, meaning "the earth". Trigonal Te with a one-dimensional (1D) structure is the energetically favored allotrope for bulk form. The crystal is formed by a parallel assembly of helical chains with three-fold screw symmetry that stretch in the z direction as shown in Fig. 1a–c, with either left- or right-handedness. Te has four 5p-orbital valence electrons in the outer shell, with two lone-pair electrons forming vdW-like inter-chain bonds, and the other two forming intra-chain covalent bonds with two neighboring Te atoms. Due to lack of inversion and mirror symmetry, two irreducible enantiomers classified as $P3_221$ or the $P3_121$ space group are distinguished by different chiralities, giving rise to many chirality-dependent properties, such as opposite spin textures[34], current-induced spin polarization[35], and circular photon drag effect[36]. The trigonal crystal structure yields a hexagonal first Brillouin zone (BZ), and density functional theory (DFT) reveals that an *almost* direct bandgap of ~0.35 eV is formed at the H points of the BZ (see Fig. 1e, f). The Fermi level is located close to the valence band, which comes from the contribution of unhybridized lone-pair $|p\rangle$ states. The doubly degenerate conduction band H_6 arises from anti-bonding of hybridized $|p\rangle$-like states. A close examination at the valence band edge suggests a camel back hump feature as depicted in Fig. 1f, which slightly shifts the wave vector of valence band maxima by less than 2% of the length of BZ.

Despite the superior electrical properties and structural advantage of tellurene for advanced CMOS technologies, the relatively low bulk bandgap poses a potential challenge to effectively shut off the transistors with a low I_{on}/I_{off} ratio compared to state-of-the-art silicon transistors. Fortunately, this issue can be mitigated by a significantly increased bandgap when the dimension of tellurene approaches 2D (few-layer) or 1D (nanowire) limit according to theoretical predictions. For example, few-layer tellurene ($N \leq 3$)[26,27,32,37] and narrow tellurene nanowires (≤ 4 nm²)[37] are predicted to have a suitable bandgap of over 1 eV. In addition, several other allotropes of tellurene that are energetically stable in monolayer form were also predicted with promising electronic properties[25,27]. However experimental

progress to synthesize these phases has been scarce so far[25,30], and its phase transition is still under investigation.

The rest of this paper will be organized as follows: in the section "Routes towards 1D and 2D tellurium", different approaches to synthesizing 1D and 2D tellurium nanostructures are summarized; in the section "Te-based CMOS and advanced device applications", we will focus on recent progress in achieving high-performance transistors and logic gates utilizing 2D Te films; the topological phases in the electronic band structure and related magneto-transport measurements will be discussed in the section "Novel physical properties in tellurium", along with other chiral-related properties and experiments; finally, we will conclude in the section "summary and outlook" and envision the future research directions for this material system.

ROUTES TOWARDS 1D AND 2D TELLURIUM

According to high-throughput vdW DFT calculations, over five thousand materials have been identified with vdW structures, yet only about 30% of them can be easily exfoliated[15]. Unfortunately, Te belongs to the majority of vdW materials which cannot be easily peeled off with the typical mechanical method using scotch tape. To explore the electrical and physical properties of Te approaching the 2D limit, other methods needed to be developed.

The one-dimensional vdW crystal structure of Te suggests the easy formation of its 1D morphology, i.e. nanowires, nanorods, nanotubes, etc. Therefore, the synthesis of 1D Te nanostructures predates its 2D counterpart. Many recent efforts of growing 2D Te films also stem from 1D growth techniques. Given that, we will first briefly review the growth of 1D Te.

Synthesis of 1D Te nanostructure

The production of Te 1D nanowires has been intensively investigated in the past two decades, motivated by its promising piezoelectric and thermoelectric properties. The mainstream growth technique is the solution-phase approach proposed by Mayers et al. in 2002[38]. 1D Te nanowires and needle-like whiskers with diameter as small as 10 nm were obtained from tellurium oxide in an ethylene glycol environment by a direct reduction process. The size, aspect ratio, and morphology can be
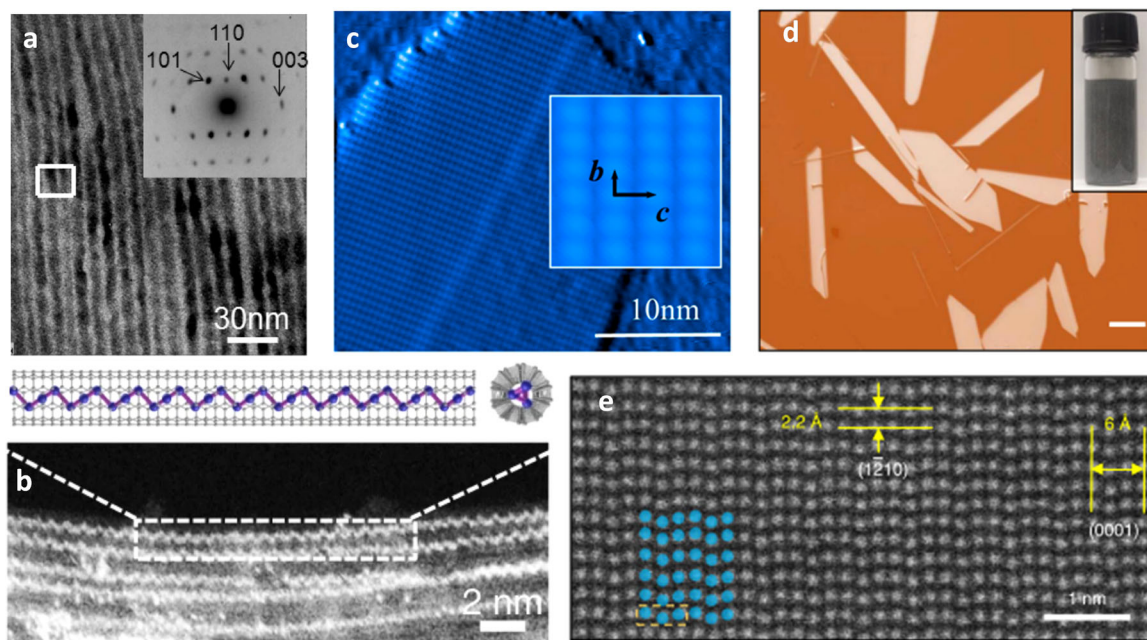
Fig. 2 Synthesis of Te 1D and 2D nanostructures. a Hydrothermally grown 1D Te nanowires with 4 nm diameter assembled by Langmuir-Blodgett technique. Reproduced from ref. [41]. **b** Single-chain 1D nanowires grown in boron nitride nanotube encapsulation. Reproduced from ref. [48]. **c** An STM image of a MBE-grown monolayer Te film on graphene. Reproduced from ref. [33]. **d** Solution-based growth of 2D tellurium films. The scale bar is 20 μm. Inset: Optical image of the Te solution dispersion. **e** An STEM image of a 2D Te film. False-colored (in blue) balls highlight the helical structure. (**d**, **e**) reproduced from ref. [32].

significantly tuned by carefully tweaking the conditions during crystal growth such as the temperature, pH value, pressure, and aqueous environment[39]. By introducing crystal-face-blocking ligand poly-vinylpyrrolidone (PVP) into the solvent-based growth medium, the uniformity and productivity of Te nanowires are significantly enhanced, while the diameter of the nanowire is reduced to as small as 4 nm[40]. These 1D nanowires can be assembled onto arbitrary substrates in parallel into continuous films with the Langmuir−Blodgett technique to harvest its photoelectric properties collectively (see Fig. 2a)[41].

Other practical routes to obtain Te nanostructures with 1D morphology were also pursued. Pioneering efforts in vapor phase synthesis date back to the 1970s[42,43], with further developments following in the last two decades[44–46]. Due to the strong interaction between inter-chain lone-pair electrons, the conventional mechanical exfoliation technique with scotch tape does not work well on Te. A tape-free exfoliation method to prepare quasi-1D Te films was recently proposed by directly scratching bulk Te on a silicon substrate[47]. Very recently, few-chain and single-chain Te nanowires were isolated and stabilized inside carbon nanotubes and boron nitride nanotubes (as shown in Fig. 2b) through a growth vapor trapping approach by Qin et al., who also demonstrated promising electrical and optical performance based on these new nanomaterial systems[48].

Growth of 2D Te films

The first reported tellurium thin films in the context of thin-film transistors were prepared by thermal evaporation in 1952[49], with more detailed growth and electrical measurements on Te thin films following in the next decade[50,51]. In the intervening years between then and the current thin film and 2D materials revolution, most of the progress made was towards increasing the grain size of the evaporated tellurium—studies suggest that grain boundary behavior can dominate tellurium's electrical properties[52,53]. In the most recent years, thin tellurium devices have seen a new spurt of growth with advanced growth methods and further improvements to film yields.

To obtain high-quality single-crystal 2D thin films, the most commonly strategies are mechanical exfoliation and chemical vapor deposition (CVD). Unfortunately, both methods have not been successful in Te films. In 2014, a vdW epitaxial growth method was proposed to circumvent this challenge[31]. Te nanoplates as thin as 30 nm were successfully grown on flexible mica substrates, with the 1D atomic chains oriented out of the 2D plane. Progress has also been made to grow monolayer tellurene films with molecular beam epitaxy (MBE) on graphite substrates as shown in Fig. 2c[30,33]. However, the graphene substrate poses challenges to perform transport characterization since it requires a complicated transfer technique to detach the monolayer Te film from the substrate. Other strategies to obtain large poly-crystalline Te films include pulsed laser deposition[54], magnetron sputtering[55], and liquid exfoliation[56]. In 2018, a breakthrough was made by Wang et al. who demonstrated a solution-based growth method to grow large-scale 2D tellurium thin films (see Fig. 2d, e)[32,33]. The technique stemmed from the earlier liquid-phase growth method of 1D tellurium nanowires[37–39]. By carefully adjusting the starting material ratio and elongating reaction time, single-crystal 2D tellurium films with lateral sizes over 100 μm and thicknesses ranging from monolayer to tens of nanometers can be obtained. By leveraging its extraordinarily high carrier mobility, large size, and capability to change the carrier density and polarity by gating, solution grown Te films opened a new chapter in exploring the material properties and exploiting the applications of Te in electronics and optoelectronics.

TE-BASED CMOS AND ADVANCED DEVICE APPLICATIONS

Despite the variety of 2D materials that have been discovered and explored, we have not yet encountered the perfect material that can replace silicon and Si-based semiconductor technology. A suitable candidate material platform should: (1) have a reasonable bandgap and sufficient I_{on}/I_{off} ratio for the device to be properly shut off for low-power applications; (2) be air-stable for real device application (instead of prototype testing devices in the lab); (3)
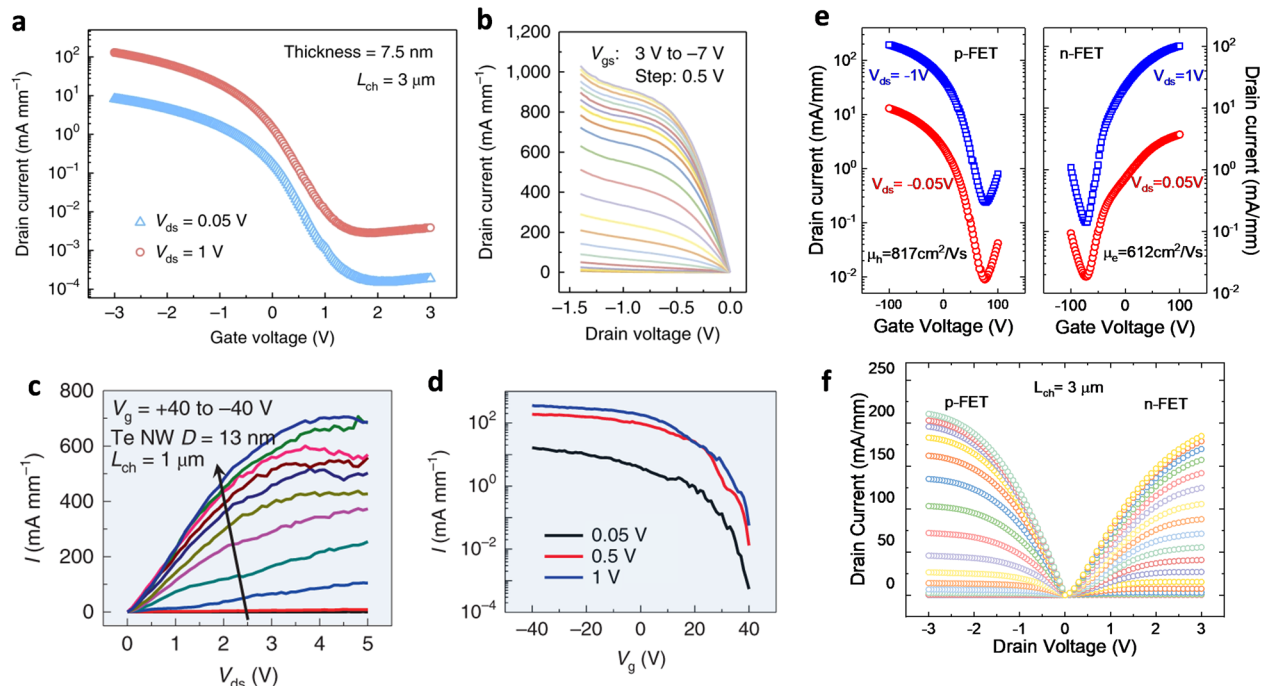
Fig. 3 2D Te thin-film transistors towards logic circuits. a Transfer curves of a typical long-channel p-FET device fabricated on a 7.5-nm-thick tellurium film. **b** Output curves of a short-channel device with drain current exceeding 1 A/mm. **a, b** reproduced from ref. [32]. **c** Tranfer and (**d**) Output characteristics of a typical boron nitride nanotube (BNNT) encapsulated Te nanowire transistor. **c, d** Reproduced from ref. [43]. **e** Transfer curves and (**f**) output curves of PMOS and NMOS devices made from 2D Te films with near-symmetric performance. The NMOS is achieved by ALD dielectric doping. **e, f** reproduced from ref. [73].

have a sophisticated doping technique for easy access to both electrons and holes in order to build complementary metal-oxide-semiconductor (CMOS) circuits; (4) have high and near-symmetric carrier mobility for both electrons and holes for building high-speed logic devices. Tellurium fulfills the requirements listed above satisfactorily. In this section, we will review the recent efforts in implementing both p-type and n-type tellurium transistors, as well as other novel device applications.

Te PMOS devices

Due to the native defects-related unintentional doping in tellurium, the Fermi level is located closer to the valence band and Te naturally exhibits p-type semiconductor behavior. Hence the realization of PMOS devices in Te is much more straightforward. In this part, we will first recap the development of Te PMOS.

Historically, evaporation-based growth methods are the most prevalent. The first thin-film tellurium FETs were reported in 1964[51], where the device performance was likely limited by small grain size. Improvements to evaporation methods came in 1971 with the discovery that very small islands of Au on the substrate act as nucleation sites for tellurium, promoting larger grain sizes up to 5 μm in diameter in samples as thin as 40 nm[57,58]. This method was later optimized[59–63] and subsequently further improved by varying the substrate temperature[64], improvements which eventually lead to the most modern evaporation method[65]. In 2020[65], Zhao et al. took advantage of the property of low substrate temperatures (−80 °C) increasing grain size to achieve wafer-scale large-grain (around 25 μm²) evaporated tellurium. The p-type transistors exhibit an on-current of roughly 1.38 mA/mm, an I_{on}/I_{off} ratio of around 10⁴, and decent subthreshold swing (SS) of 108 mV/dec. These devices are applied to large and multi-layer logic circuits, which will be discussed in more depth later.

Besides direct evaporation of Te onto substrates, there are some other related methods. Recently, Te thin films evaporated from ZrTe₂ powder onto sapphire substrates have been used to grow

flakes as thin as 3 nm, with a fabricated device yielding a reasonably high field-effect mobility of 349 cm²/V s on a 21 nm thick flake[66]. However, the device suffers from low I_{on}/I_{off} ratio. Another related method that has been reported is CVD from a TeO₂ source in a hydrogen atmosphere[67], where the device performance is also inferior to films grown by other methods to date.

Shortly after the hydrothermal growth method was developed[68], high-quality single-crystal 2D tellurium p-FETs were demonstrated with hole field-effect mobility near 700 cm²/V s[32,69]. These initial devices showed an I_{on}/I_{off} ratio of around 10⁵ with an on-current greater than 300 mA/mm using the back-gated FET configuration (see Fig. 3a). By taking advantage of channel scaling and high-k ALD-deposited dielectrics, an improved on-current above 1 A/mm was achieved, as demonstrated in Fig. 3b. These Te transistors also exhibit outstanding air-stability over two months' time span. At present, this hydrothermal method still produces the best transistor characteristics.

One challenge that tellurene transistors may face is the low I_{on}/I_{off} ratio that inherently arises from its relatively narrow bulk bandgap (0.35 eV). So far, the highest I_{on}/I_{off} ratio reported in tellurene transistors barely exceeds 10⁶ [32], which might be acceptable in some specific applications, but still inferior to the state-of-the-art silicon devices. In highly integrated electronics, a high off-state current will cause large standby power consumption and poses serious challenges to thermal management. One potential solution to this issue, is to scale the tellurene dimension down to the quantum limit to increase the bandgap[26,27,32,37]. The ultra-scaled tellurene promises improved device performance in different device architectures such as dual-gated planar transistors[70] and gate-all-around nanowire transistors[71] beyond sub-5 nm technology nodes.

It is worth mentioning that PMOS devices were also explored in 1D Te nanostructures, with potential applications for future ultra-scaled FinFETs. MBE-grown quasi-1D nanorods exhibit an extra-ordinary high mobility of 707 cm²/V s in a 235 nm wide

nanowire[72]. By encapsulating Te nanowires in boron nitride nanotubes (BNNT), by far the thinnest 1D Te-based FET devices with a diameter of 2 nm were demonstrated by Qin et al.[48]. A representative BNNT-encapsulated 1D Te nanowire transistor exhibits p-type transport behavior with an on/off ratio over 10^4 and an on-state current over 700 mA/mm (see Fig. 3c, d). These encapsulated 1D Te devices also show exceptionally large current carrying capacity of 1.5×10^8 A cm^{-2}.

N-type doping and logic gates

To construct CMOS circuits with both NMOS and PMOS operating with near-symmetric performance, a controllable doping technique is essential. For silicon, sophisticated doping strategies, mainly implantation and diffusion, have been well-developed in the last several decades. However, for the rising 2D materials lack of effective doping methods has always been a major obstacle towards commercialization. Most materials, such as MoS_2 and black phosphorus, show superb electrical performance in one carrier species yet can hardly be tuned to the other polarity. In some other 2D materials like $ReSe_2$ the Fermi level is located close to the middle of the bandgap and thus both p-type and n-type branches suffer from large Schottky barriers and low on-state current.

Tellurium can be made n-type through the addition of certain atomic layer deposited (ALD) dielectrics as confirmed by transport measurements[73] and near-field scanning microwave microscopy[74]. Although the physical mechanism behind the doping effect is not entirely clear, the authors suggest that it may be due to fixed charges in the dielectric media. Using low work function metal contacts (Ti), high drive currents and field-effect mobilities (~200 mA/mm in a long-channel device with $L_{ch} = 3$ μm, and 612 cm^2/V s respectively) were reported in ALD-doped NMOS devices, with very symmetric performance to the native p-type devices as shown in Fig. 3e, f. This doping strategy also enabled the investigation of quantum transport of conduction band electrons recently[75,76].

To date, few results have been reported for logic circuits with modern tellurium growth methods. This is likely due in part to the difficulty of obtaining large-area high-quality single-crystalline films and in part to the difficulty of fabricating CMOS circuits on Te (although a route towards doing that has recently opened, and a prototypical CMOS inverter was demonstrated[73]). An early paper reported using thin-film Te (in tandem with Se or CdS) in a scan generator implementation[77]. An inverter made solely from PMOS with a gain of 22 at $V_{dd} = 1$ V and 38 at $V_{dd} = 2$ V is shown with evaporated Te films[65]. More complicated NAND gates were fabricated and combined with the PMOS inverters to demonstrate a full adder and 2-bit multiplier[65]. The ability to stack layers of evaporated transistors without significant device degradation and device stability under repeated strain for flexible electronics applications are also demonstrated[65].

Applications beyond electronics

Combining its high quality, large size, and unique intrinsic properties, tellurium films promise versatile applications beyond logic devices. For instance, with a direct bandgap of 0.35 eV, highly sensitive photo-response was achieved in a 2D tellurium-based photodetector operating in a broadband[31,78–80] up to mid-infrared regime[69,81]. Strong angle-dependent optical response due to its inherent structural anisotropy was also reported in 2D Te[32,81,82], which opens a potential pathway for designing novel polarized imaging optoelectronics.

Its non-centrosymmetric structure gives rise to a strong piezoelectric effect in Te[83,84]. By reducing the dimensionality, stronger asymmetry is induced in Te films and thus the piezoelectric effect can be further enhanced. Piezoelectric and triboelectric nanogenerator devices have been implemented with 1D Te nanowire arrays[85,86] and 2D films[87].

Tellurium[88,89] and its telluride compounds[90] are also among the top materials for thermoelectric performance, as its heavy atoms have strong interactions with phonons to suppress thermal conductivity. In the last two decades, going low-dimensional has become an emerging trend to further enhance thermoelectric performance[91–93]. By carefully choosing the characteristic length of the nanostructure, the Wiedemann–Franz law which links thermal conductivity and electric conductivity of the material can be overthrown in Te. High thermoelectric performance was predicted in 2D Te films in recent years[94–96], which was experimentally demonstrated in 2019 with a thermoelectric figure of merit ZT of 0.63 at room temperature[97].

NOVEL PHYSICAL PROPERTIES IN TELLURIUM

SdH oscillations and quantum Hall effect

Under strong magnetic fields and at low temperatures, discrete energy levels form in tellurium's electronic band structure due to Landau quantization, resulting in oscillations in the conductivity of the material, known as Shubnikov–de Haas (SdH) oscillations. This effect is commonly used as a powerful technique to create a portrait of the Fermi surface of a material, as the oscillation frequency is associated with the Fermi surface area according to the Onsager rule.

The earliest documentation of SdH oscillations in bulk Te can be traced back to 1968[98], followed by a comprehensive investigation of the Fermi surface in the Te valence band in the next decade[99–103]. Thanks to the high crystal quality, the famous "camel back" feature (Fig. 1f) in the vicinity of valence band maxima was well captured with two separate Fermi pockets at extremely low carrier density, which merge together at a density of around 10^{17} cm^{-3} [98,99]. Due to the native p-type doping, most of the magneto-transport measurements were carried out in the valence band of Te. In 1975, the conduction band of Te was first accessed in a surface inversion layer by treating the specimen with a hydrofluoric acid-based solution[104]. Quantum oscillations were reported in the conduction band electrons subsequently[104,105]. Given the weak quantization without 2D confinement, the oscillation patterns were only revealed by taking the second derivative of magnetoresistance in most cases.

SdH oscillations are the prelude to the quantum Hall effect (QHE), if strong 2D confinement is imposed. In the quantum Hall regime, the Hall resistance (R_{xy}) is quantized to an integer fraction of h/e^2, where h is Planck's constant and e is the elementary charge, and the longitudinal resistance (R_{xx}) vanishes due to back-scattering free edge channels. In retrospect of K. von Klitzing's discovery of the QHE in 1980[4], we can conclude the prerequisites for observing QHE are: (i) high carrier mobility, (ii) low temperature, (iii) strong external magnetic field, and (iv) a 2D electron gas (2DEG) system. Interestingly, 9 years prior to his Nobel prize-winning discovery in silicon MOSFETs, von Klitzing also observed quantum oscillations in tellurium surface states[103]. By that time Te samples exhibited high carrier mobility comparable to silicon, and the experiments were performed in a low-T high-B environment. The only missing piece of the puzzle was the strong 2D quantum confinement, which could have led the groundbreaking discovery nearly a decade earlier. After near half a century, the QHE was observed in hydrothermally grown 2D Te films for the first time (Fig. 4a). The p-type films had a measured hole mobility of 2400 cm^2/Vs at ^{3}He temperature. Landau levels with four-fold degeneracy are attributed to the spin and valley (H and H' points in the BZ) degeneracies[106]. Angle-dependent SdH measurements reveal that the oscillation frequency follows a 1/cos (θ) relation with tilted angles as shown in Fig. 4b, suggesting that the Landau quantization only responds to the perpendicular
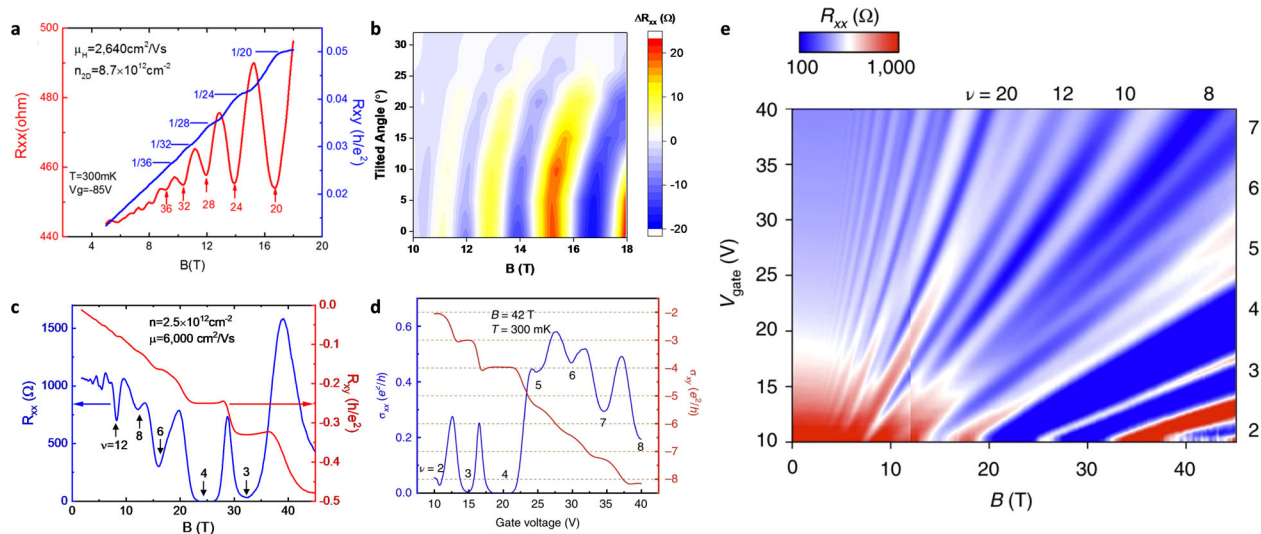
Fig. 4   SdH oscillations and quantum Hall effect in 2D Te. a SdH oscillations in p-type 2D Te with four-fold degeneracy. **b** Oscillation patterns as a function of B field show $1/\cos(\theta)$ dependence on tilt angle, suggesting the formation of 2D Fermi surface. (**a**, **b**) are reproduced from ref. [106]. **c** Magnetic field dependence and (**d**) gate dependence of quantum Hall effect in n-type 2D Te. The 2D electron gas enters the fully quantized regime at filling factors of 3 and 4, with all degeneracies being lifted. **e** Landau fan mapping of SdH and quantum Hall effect in n-type Te in the gate voltage-B field parameter space. (**c**–**e**) are reproduced from ref. [76].

magnetic field. This indicates the Fermi surface is in the 2D limit, which is distinctive from previous bulk SdH measurements. Later enabled by the development of n-type ALD dielectric doping in 2D Te, the QHE was further demonstrated in 2DEGs in the conduction band of Te with an electron mobility of 6000 cm²/V s[76]. In n-type 2D Te films, all degeneracies were lifted under high magnetic field, as described in Fig. 4c, d. Pronounced SdH oscillations and well-developed quantum Hall states are mapped out in a Landau fan diagram in Fig. 4e. Surprisingly, a non-trivial π Berry phase was detected, due to the Kramers–Weyl nodes at the bottom of the conduction band. These Kramers-Weyl nodes originate from the chiral crystal structure of Te, as will be elaborated next.

Topological phases of tellurium

The recent renaissance of Te is also partly credited to its topological features in the band structure. Te was first proposed to undergo a transition from a trivial insulator to a Weyl semimetal or a topological insulator under pressure, as described in Fig. 5a–c[107,108]. Under ambient pressure, Te is a gapped trivial insulator. The bandgap decreases by increasing the pressure until the valence band and conduction band touch each other to form a semimetal phase. This prediction is backed by Fermi surface evolution measurements from SdH oscillations at pressures up to 3 GPa[109]. A superconducting state is also observed in the metallic phase of Te above 4 GPa[110,111]. Recently, optical evidence of the Weyl semimetal phase transition was found using high-pressure infrared spectroscopy[112,113]. By measuring the optical conductivity at different pressures, two linear regimes are found in the Weyl semimetal phase of Te (Fig. 5d).

Another emerging subject on the topological properties of Te is the intrinsic Weyl nodes under ambient pressure. Large spin-splitting in the valence bands is predicted and observed in angle-resolved photoemission spectroscopy (ARPES) measurements[114] as a direct consequence of strong spin-orbit coupling (SOC) and the broken inversion symmetry of tellurium's chiral crystal structure. These spin-polarized bands form multiple Weyl nodes with two different origins: accidental band crossing between the H_5 and H_6 bands along the H-K line (denoted as P_1 in Fig. 5a) and Kramers–Weyl nodes due to the chiral symmetry of the crystal (two circles at the H points in Fig. 5a)[108,114]. Despite the different

mechanisms of formation, these Weyl nodes have the same topological properties in the sense that they all act as monopoles of effective magnetic field (Berry curvature) in momentum space[115]. The Weyl nodes at the H and H' points are of particular interest to recent research since they arise at high symmetry points of a chiral crystal with screw symmetry in the presence of strong SOC. These Weyl nodes are classified as Kramers–Weyl nodes as the double degeneracy is protected by Kramers theorem due to the chiral crystal structure[116]. These Weyl nodes have some unique topological features such as exceptionally large energy windows for observing topological order[116], and radial spin textures around the source and sink of Berry curvature[34,108]. Chiral-anomaly-induced negative magnetoresistance and planar Hall effect were reported (Fig. 5e) which might be related to the Weyl fermions in p-type Te[117]. However, the direct transport manifestation of Weyl nodes in the valence band is challenging, due to the fact that these Weyl nodes are embedded deep in the valence band far away from the Fermi surface and thus have little contribution to carrier transport. With the recent progress in n-type doping of Te 2D films, the Kramers-Weyl nodes in the lowest unoccupied states of the H_6 bands have also become available. These Weyl nodes are only several meV away from the conduction band minima, allowing the chemical potential to be continuously modulated near Weyl points which is highly desirable to study Weyl physics and implement topological devices. Non-trivial π Berry phase was detected in the quantum Hall sequences (see Fig. 5f, g), providing direct proof of the existence of Weyl fermions in n-type Te[76].

Chiral structure and related properties

Chiral crystals and their structure-property correspondence are rising as a significant ingredient for realizing novel topological orders and designing new device concepts[116,118]. The non-symmorphic chiral structure of Te is described by a three-fold rotational symmetry plus a translational symmetry along its z-axis. Depending on the rotating directions of the helical chains, the Te crystals can be categorized into two irreducible space groups, $P3_121$ or $P3_221$, which are linked by a mirror operation, as indicated in Fig. 6a. A chemical method was developed in 1970 to rapidly determine the chirality of Te crystals[119,120]. Hot sulfuric acid will slowly react with the surface, leaving asymmetric etching
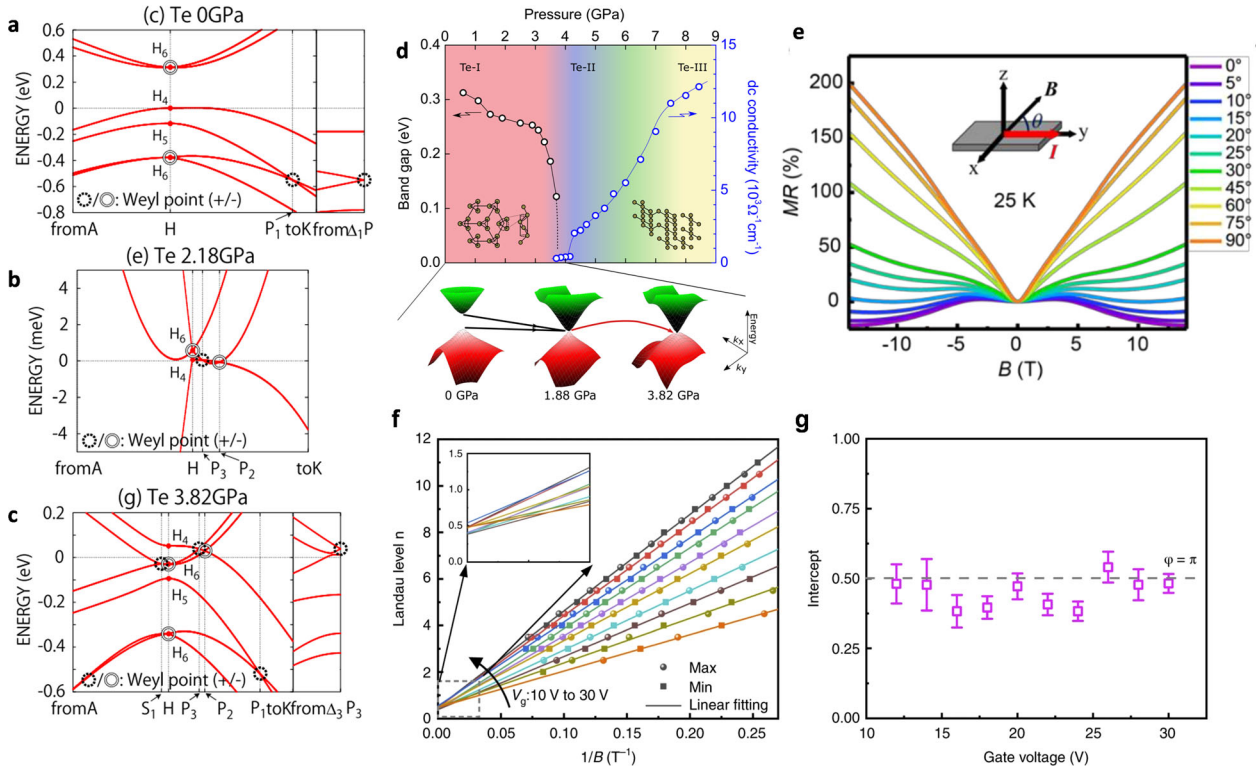
Fig. 5 **Topological properties of Te. a–c** Topological transitions of Te electronic structures under pressures of 0, 2.18, and 3.82 GPa, respectively. Without pressure, Weyl nodes on the H-K line from accidental crossing and Kramers-Weyl nodes at the H point are present, along with a trivial bandgap near the Fermi level. It undergoes a transition from trivial insulator to Weyl semimetal with increased pressure. (**a–c**) reproduced from ref. [108]. **d** Experimental evidence of topological phase transition under pressure from infrared response and X-ray diffraction. Reproduced from ref. [113]. **e** Chiral anomaly induced negative magnetoresistance in p-type bulk Te as evidence of Weyl nodes in the valence band. Reproduced from ref. [117]. **f, g** Landau fan diagram constructed from SdH oscillation sequences in n-type 2D Te film with non-trivial π Berry phase as a manifestation of Weyl nodes near conduction band edge. (**f, g**) reproduced from ref. [76].
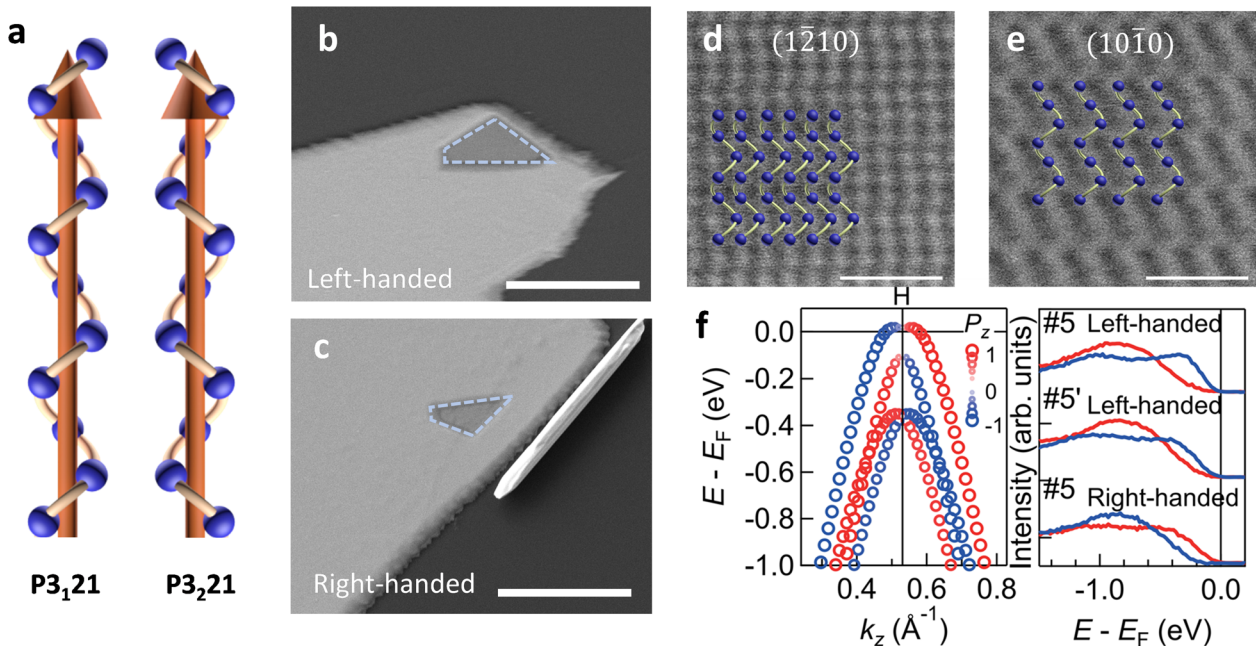

Fig. 6 **Chirality and chirality-related properties in Te. a** left-handed and right-handed Te helical chains (space group P3$_1$21 and P3$_2$21) linked by mirror transformation. **b, c** Asymmetric etching pits on Te surface from hot sulfuric acid etching as a rapid way to identify the chirality of Te. Scale bars: 5 μm. **d, e** Direct visualization of Te chirality by HRTEM technique from different crystal facets. Scale bars: 1 nm. **f** Opposite spin textures near the H point in the valence band in left-handed and right-handed Te measured from spin-resolved ARPES. (**f**) is reproduced from ref. [34].

pits (as shown in Fig. 6b, c), the shapes of which are determined by the handedness of the chiral structure. By cross-checking with nuclear magnetic resonance (NMR) spectroscopy, one can easily associate the chirality with the shape of etching pits. Alternatively, the atomic-level chirality can be directly imaged with aberration-corrected scanning TEM along different zone axes[121], as exemplified in Fig. 6d, e. By combining two TEM images along, for instance, $[1\bar{2}10]$ and $[10\bar{1}0]$ zone axes, the atomic arrangement can be holographically imaged to identity chirality.

The three-fold screw symmetry breaks the spatial inversion symmetry, and along with the strong SOC this gives rise to many other chirality-related phenomena in Te. For example, the previously mentioned Kramers–Weyl nodes[76] only exist in chiral material systems with strong SOC[116]. Many magnetoelectric effects were discovered in Te which also originates from its chiral structure. For example, current-induced magnetization was reported in both the orbital and spin angular momentum of Te[122–124]; strong electrical magneto-chiral anisotropy was also experimentally demonstrated[125]. Spin-resolved ARPES reveals that the radial spin texture in the valence band of Te is also chirality-dependent (Fig. 6f)[34]. This radial spin texture gives rise to current-induced spin polarization[35], which can be potentially exploited in spintronics. The current-induced spin polarization in Te has a similar mechanism to the Rashba–Edelstein effect, except that in the case of Te the spin is polarized in parallel to the injecting current direction[114].

SUMMARY AND OUTLOOK

In this paper, we summarized the recent research boom of Te as an elemental low-dimensional van der Waals material. Bulk Te exhibits exotic physical properties and novel topological phases associated with its chiral structure. The desire to investigate these properties in reduced dimensions has spurred significant advancements in the synthesis of Te nanostructures including 1D nanowires and 2D films. Particularly by leveraging the large size and high carrier mobility of 2D tellurium films grown by a hydrothermal process, this material platform has demonstrated versatile functionalities and potential applications for electronics, optoelectronics, piezo-electronics, thermoelectric devices, spintronics, and quantum devices. Based on the recent progress, we anticipate future Te research will be focused on the following subjects: (1) optimizing material growth techniques towards higher quality atomically thin 2D films and atomically wide 1D nanowires; (2) implementing ultra-scaled planar Te CMOS transistors and 3D FETs based on 1D Te nanowires; (3) designing optoelectronics, wearable electronics, synaptic devices, tribo-electric nanogenerators, and other device concepts with novel functionalities and enhanced performance; (4) investigating transport and quantum behavior in low-dimensional confinement with reduced symmetry; (5) manipulating chirality-related properties, particularly chirality-dependent radial spin textures for potential spintronic applications. We envision low-dimensional Te to be a focal point in material science, electronic devices, and condensed-matter physics for years to come.

Reporting summary

Further information on research design is available in the Nature Research Reporting Summary linked to this article.

DATA AVAILABILITY

Data sharing is not applicable to this paper, as no original datasets were generated or analyzed for this review.

REFERENCES

1. Chhowalla, M., Jena, D. & Zhang, H. Two-dimensional semiconductors for transistors. *Nat. Rev. Mater.* **1**, 16052 (2016).
2. Novoselov, K. S., Mishchenko, A., Carvalho, A. & Castro Neto, A. H. et al. 2D materials and van der Waals heterostructures. *Science* **353**, aac9439 (2016).
3. Geim, A. K. & Grigorieva, I. V. Van der Waals heterostructures. *Nature* **499**, 419–425 (2013).
4. Klitzing, K. V., Dorda, G. & Pepper, M. New method for high-accuracy determination of the fine-structure constant based on quantized Hall resistance. *Phys. Rev. Lett.* **45**, 494–497 (1980).
5. Zhang, Y., Tan, Y.-W., Stormer, H. L. & Kim, P. Experimental observation of the quantum Hall effect and Berry's phase in graphene. *Nature* **438**, 201–204 (2005).
6. Novoselov, K. S. et al. Room-temperature quantum Hall effect in graphene. *Science* **315**, 1379–1379 (2007).
7. Novoselov, K. S. et al. Two-dimensional gas of massless Dirac fermions in graphene. *Nature* **438**, 197–200 (2005).
8. Castro Neto, A. H., Guinea, F., Peres, N. M. R., Novoselov, K. S. & Geim, A. K. The electronic properties of graphene. *Rev. Mod. Phys.* **81**, 109–162 (2009).
9. Cao, Y. et al. Correlated insulator behaviour at half-filling in magic-angle graphene superlattices. *Nature* **556**, 80–84 (2018).
10. Cao, Y. et al. Unconventional superconductivity in magic-angle graphene superlattices. *Nature* **556**, 43–50 (2018).
11. Hunt, B. et al. Massive Dirac fermions and Hofstadter butterfly in a van der Waals heterostructure. *Science* **340**, 1427–1430 (2013).
12. Tang, S. et al. Quantum spin Hall state in monolayer 1T'-WTe 2. *Nat. Phys.* **13**, 683–687 (2017).
13. Deng, Y. et al. Quantum anomalous Hall effect in intrinsic magnetic topological insulator MnBi$_2$Te$_4$. *Science* **367**, 895–Te900 (2020).
14. Liu, C. et al. Robust axion insulator and Chern insulator phases in a two-dimensional antiferromagnetic topological insulator. *Nat. Mater.* **19**, 522–527 (2020). *arXiv preprint arXiv:1905.00715* (2019).
15. Mounet, N. et al. Two-dimensional materials from high-throughput computational exfoliation of experimentally known compounds. *Nat. Nanotechnol.* **13**, 246–252 (2018).
16. Novoselov, K. S. et al. Electric field effect in atomically thin carbon films. *Science* **306**, 666–669 (2004).
17. Li, L. et al. Black phosphorus field-effect transistors. *Nat. Nanotechnol.* **9**, 372 (2014).
18. Liu, H. et al. Phosphorene: an unexplored 2D semiconductor with a high hole mobility. *ACS Nano* **8**, 4033–4041 (2014).
19. Dávila, M. E., Xian, L., Cahangirov, S., Rubio, A. & Le Lay, G. Germanene: a novel two-dimensional germanium allotrope akin to graphene and silicene. *N. J. Phys.* **16**, 095002 (2014).
20. Bampoulis, P. et al. Germanene termination of Ge2Pt crystals on Ge(110). *J. Condens. Matter Phys.* **26**, 442001 (2014).
21. Sone, J., Yamagami, T., Aoki, Y., Nakatsuji, K. & Hirayama, H. Epitaxial growth of silicene on ultra-thin Ag(111) films. *N. J. Phys.* **16**, 095004 (2014).
22. Ahmed, R., Nakagawa, T. & Mizuno, S. Structure determination of ultra-flat stanene on Cu(111) using low energy electron diffraction. *Surf. Sci.* **691**, 121498 (2020).
23. Yuhara, J. et al. Large area planar stanene epitaxially grown on Ag(1 1 1). *2D Mater.* **5**, 025002 (2018).
24. Reis, F. et al. Bismuthene on a SiC substrate: a candidate for a high-temperature quantum spin Hall material. *Science* **357**, 287–290 (2017).
25. Zhu, Z. et al. Multivalency-driven formation of Te-based monolayer materials: a combined first-principles and experimental study. *Phys. Rev. Lett.* **119**, 106101 (2017).
26. Wu, B., Liu, X., Yin, J. & Lee, H. Bulkβ-Te to few layeredβ-tellurenes: indirect to direct band-gap transitions showing semiconducting property. *Mater. Res. Express* **4**, 095902 (2017).
27. Qiao, J. et al. Few-layer tellurium: one-dimensional-like layered elementary semiconductor with striking physical properties. *Sci. Bull.* **63**, 159–168 (2018).
28. Wang, C. et al. Charge-governed phase manipulation of few-layer tellurium. *Nanoscale* **10**, 22263–22269 (2018).
29. Reed, E. J. Two-dimensional tellurium. *Nature* **552**, 40–41 (2017).
30. Chen, J. et al. Ultrathin β-tellurium layers grown on highly oriented pyrolytic graphite by molecular-beam epitaxy. *Nanoscale* **9**, 15945–15948 (2017).
31. Wang, Q. et al. Van der Waals epitaxy and photoresponse of hexagonal tellurium nanoplates on flexible mica sheets. *ACS Nano* **8**, 7497–7505 (2014).

32. Wang, Y. et al. Field-effect transistors made from solution-grown two-dimensional tellurene. *Nat. Electron.* **1**, 228–236 (2018).

33. Huang, X. et al. Epitaxial Growth and Band Structure of Te Film on Graphene. *Nano Lett.* **17**, 4619–4623 (2017).

34. Sakano, M. et al. Radial spin texture in elemental tellurium with chiral crystal structure. *Phys. Rev. Lett.* **124**, 136404 (2020).

35. Shalygin, V., Sofronov, A., Vorob'ev, L. & Farbshtein, I. Current-induced spin polarization of holes in tellurium. *Phys. Solid State* **54**, 2362–2373 (2012).

36. Shalygin, V., Moldavskaya, M., Danilov, S., Farbshtein, I. & Golub, L. Circular photon drag effect in bulk tellurium. *Phys. Rev. B* **93**, 045207 (2016).

37. Kramer, A., Van de Put, M. L., Hinkle, C. L. & Vandenberghe, W. G. Tellurium as a successor of silicon for extremely scaled nanowires: a first-principles study. *NPJ 2D Mater. Appl* **4**, 10 (2020).

38. Mayers, B. & Xia, Y. One-dimensional nanostructures of trigonal tellurium with various morphologies can be synthesized using a solution-phase approach. *J. Mater. Chem.* **12**, 1875–1881 (2002).

39. Mo, M. et al. Controlled hydrothermal synthesis of thin single-crystal tellurium nanobelts and nanotubes. *Adv. Mater.* **14**, 1658–1662 (2002).

40. Qian, H.-S., Yu, S.-H., Gong, J.-Y., Luo, L.-B. & Fei, L.-F. High-quality luminescent tellurium nanowires of several nanometers in diameter and high aspect ratio synthesized by a poly (vinyl pyrrolidone)-assisted hydrothermal process. *Langmuir* **22**, 3830–3835 (2006).

41. Liu, J.-W., Zhu, J.-H., Zhang, C.-L., Liang, H.-W. & Yu, S.-H. Mesostructured assemblies of ultrathin superlong tellurium nanowires and their photoconductivity. *J. Am. Chem. Soc.* **132**, 8945–8952 (2010).

42. Furuta, N. & Wada, N. Tellurium and thallium-telluride whiskers grown by the vapor-liquid-solid (VLS) process. *Jpn. J. Appl. Phys.* **11**, 1753–1754 (1972).

43. Furuta, N., Itinose, H., Maruyama, N. & Ohasi, Y. Morphology and dislocation structure of tellurium whiskers grown from the vapor. *Jpn. J. Appl. Phys.* **11**, 1113 (1972).

44. Geng, B., Lin, Y., Peng, X., Meng, G. & Zhang, L. Large-scale synthesis of single-crystalline Te nanobelts by a low-temperature chemical vapour deposition route. *Nanotechnology* **14**, 983 (2003).

45. Safdar, M. et al. Site-specific nucleation and controlled growth of a vertical tellurium nanowire array for high performance field emitters. *Nanotechnology* **24**, 185705 (2013).

46. Li, X.-L., Cao, G.-H., Feng, C.-M. & Li, Y.-D. Synthesis and magnetoresistance measurement of tellurium microtubes. *J. Mater. Chem.* **14**, 244–247 (2004).

47. Churchill, H. O. H. et al. Toward single atom chains with exfoliated tellurium. *Nanoscale Res. Lett.* **12**, 488 (2017).

48. Qin, J.-K. et al. Raman response and transport properties of tellurium atomic chains encapsulated in nanotubes. *Nat. Electron.* **3**, 141–147 (2020).

49. Aigrain, P., Lagrenaudie, J. & Liandrat, G. Modulation de la conductance d'un semi-conducteur par un champ électrique. *J. Phys. Radium* **13**, 587–588 (1952).

50. Ghosh, S. Variation of field effect mobility and Hall effect mobility with the thickness of the deposited films of tellurium. *J. Phys. Chem. Solids* **19**, 61–65 (1961).

51. Weimer, P. K. A p-type tellurium thin-film transistor. *Proc. IEEE* **52**, 608–609 (1964).

52. Phahle, A. M. Electrical properties of thermally evaporated tellurium films. *Thin solid films* **41**, 235–241 (1977).

53. Capers, M. J. & White, M. The electrical properties of vacuum deposited tellurium films. *Thin solid films* **15**, 5–14 (1973).

54. Apte, A. et al. Polytypism in ultrathin tellurium. *2d Mater.* **6**, 015013 (2018).

55. Bianco, E. et al. Large-area ultrathin Te films with substrate-tunable orientation. *Nanoscale* **12**, 12613–12622 (2020).

56. Xie, Z. et al. Ultrathin 2D nonlayered tellurium nanosheets: facile liquid-phase exfoliation, characterization, and photoresponse with high performance and enhanced stability. *Adv. Funct. Mater.* **28**, 1705833 (2018).

57. Dutton, R. W. & Muller, R. S. Electrical properties of tellurium thin films. *Proc. IEEE* **59**, 1511–1517 (1971).

58. Dutton, R. & Muller, R. Large grain tellurium thin films. *Thin Solid Films* **11**, 229–236 (1972).

59. Okuyama, K., Yamamoto, H. & Kumagai, Y. Effect of Au nucleation centers and deposition rate on crystallinity and electronic properties of evaporated Te films. *J. Appl. Phys.* **46**, 105–111 (1975).

60. Okuyama, K. & Watanabe, Y. Effect of predeposited Ag, Sn, Bi, Al and Se nucleation centers on the grain growth of evaporated Te films. *Jpn. J. Appl. Phys.* **15**, 1881 (1976).

61. Okuyama, K., Yamashita, T., Chiba, M. & Kumagai, Y. Annealing effect in tellurium films. *Jpn. J. Appl. Phys.* **16**, 1571 (1977).

62. De Vos, A. & Aerts, J. The influence of deposition rate on the electrical properties of thin tellurium films. *Thin Solid Films* **46**, 223–228 (1977).

63. Okuyama, K. & Kudo, H. Improved tellurium films by partially ionized vapor deposition as the semiconductor layer of a TFT and a hydrogen sensor. *Jpn. J. Appl. Phys.* **28**, 770 (1989).

64. Okuyama, K. & Kumagai, Y. Grain growth of evaporated Te films on a heated and cooled substrate. *J. Appl. Phys.* **46**, 1473–1477 (1975).

65. Zhao, C. et al. Evaporated tellurium thin films for p-type field-effect transistors and circuits. *Nat. Nanotechnol.* **15**, 53–58 (2020).

66. Sapkota, K. R., Lu, P., Medlin, D. L. & Wang, G. T. High temperature synthesis and characterization of ultrathin tellurium nanostructures. *APL Mater.* **7**, 081103 (2019).

67. Zhang, X. et al. Hydrogen-assisted growth of ultrathin Te flakes with giant gate-dependent photoresponse. *Adv. Funct. Mater.* **29**, 1906585 (2019).

68. Du, Y. et al. One-dimensional van der waals material tellurium: raman spectroscopy under strain and magneto-transport. *Nano Lett.* **17**, 3965–3973 (2017).

69. Amani, M. et al. Solution-synthesized high-mobility tellurium nanoflakes for short-wave infrared photodetectors. *ACS Nano* **12**, 7253–7263 (2018).

70. Yan, J. et al. Excellent device performance of sub-5-nm monolayer tellurene transistors. *Adv. Electron. Mater.* **5**, 1900226 (2019).

71. Yin, Y. et al. Tellurium nanowire gate-all-around MOSFETs for sub-5 nm applications. *ACS Appl. Mater. Interfaces* **13**, 3387–3396 (2021).

72. Zhou, G. et al. High-mobility helical tellurium field-effect transistors enabled by transfer-free, low-temperature direct growth. *Adv. Mater.* **30**, 1803109 (2018).

73. Qiu, G. et al. High-performance few-layer tellurium CMOS devices enabled by atomic layer deposited dielectric doping technique. *IEEE Device Res. Conf.* 1-2, https://ieeexplore.ieee.org/abstract/document/8442253 (2018).

74. Berweger, S. et al. Imaging carrier inhomogeneities in ambipolar tellurene field effect transistors. *Nano Lett.* **19**, 1289–1294 (2019).

75. Niu, C. et al. Gate-tunable strong spin-orbit interaction in two-dimensional tellurium probed by weak antilocalization. *Phys. Rev. B* **101**, 205414 (2020).

76. Qiu, G. et al. Quantum Hall effect of Weyl fermions in n-type semiconducting tellurene. *Nat. Nanotechnol. J. Abbr.* **15**, 585–591 (2020).

77. Weimer, P., Borkan, H., Sadasiv, G., Meray-Horvath, L. & Shallcross, F. Integrated circuits incorporating thin-film active and passive elements. *Proc. IEEE* **52**, 1479–1486 (1964).

78. Rui, C. et al. Solar-blind deep-ultraviolet photodetectors based on solution-synthesized quasi-2D Te nanosheets. *Nanophotonics* **9**, 2459–2466 (2020).

79. Kang, S. et al. Broad spectral response of an individual tellurium nanobelt grown by molecular beam epitaxy. *Nanoscale* **11**, 1879–1886 (2019).

80. Shen, C. et al. Tellurene photodetector with high gain and wide bandwidth. *ACS Nano* **14**, 303–310 (2020).

81. Tong, L. et al. Stable mid-infrared polarization imaging based on quasi-2D tellurium at room temperature. *Nat. Commun.* **11**, 2308 (2020).

82. Jnawali, G. et al. Ultrafast photoinduced band splitting and carrier dynamics in chiral tellurium nanosheets. *Nat. Commun.* **11**, 1–10 (2020).

83. Royer, D. & Dieulesaint, E. Elastic and piezoelectric constants of trigonal selenium and tellurium crystals. *J. Appl. Phys.* **50**, 4042–4045 (1979).

84. Arlt, G. & Quadflieg, P. Electronic displacement in tellurium by mechanical strain. *Phys. Status Solidi (b)* **32**, 687–689 (1969).

85. Wang, Y. et al. Scalable nanomanufacturing and assembly of chiral-chain piezoelectric tellurium nanowires for wearable self-powered cardiovascular monitoring. *Nano Futures* **3**, 011001 (2019).

86. Lee, T. I. et al. High-power density piezoelectric energy harvesting using radially strained ultrathin trigonal tellurium nanowire assembly. *Adv. Mater.* **25**, 2920–2925 (2013).

87. He, W. et al. Synthesis of ultra-thin tellurium nanoflakes on textiles for high-performance flexible and wearable nanogenerators. *Appl. Surf. Sci.* **392**, 1055–1061 (2017).

88. Peng, H., Kioussis, N. & Snyder, G. J. Elemental tellurium as a chiral p-type thermoelectric material. *Phys. Rev. B* **89**, 195206 (2014).

89. Lin, S. et al. Tellurium as a high-performance elemental thermoelectric. *Nat. Commun.* **7**, 10287 (2016).

90. Wright, D. Thermoelectric properties of bismuth telluride and its alloys. *Nature* **181**, 834–834 (1958).

91. Venkatasubramanian, R., Siivola, E., Colpitts, T. & O'quinn, B. Thin-film thermoelectric devices with high room-temperature figures of merit. *Nature* **413**, 597–602 (2001).

92. Dresselhaus, M. S. et al. New directions for low-dimensional thermoelectric materials. *Adv. Mater.* **19**, 1043–1053 (2007).

93. Heremans, J. P., Dresselhaus, M. S., Bell, L. E. & Morelli, D. T. When thermoelectrics reached the nanoscale. *Nat. Nanotechnol.* **8**, 471–473 (2013).

94. Gao, Z., Tao, F. & Ren, J. Unusually low thermal conductivity of atomically thin 2D tellurium. *Nanoscale* **10**, 12997–13003 (2018).

95. Lin, C., Cheng, W., Chai, G. & Zhang, H. Thermoelectric properties of two-dimensional selenene and tellurene from group-VI elements. *Phys. Chem. Chem. Phys.* **20**, 24250–24256 (2018).

96. Sharma, S., Singh, N. & Schwingenschlögl, U. Two-dimensional tellurene as excellent thermoelectric material. *ACS Appl. Energy Mater.* **1**, 1950–1954 (2018).

97. Qiu, G. et al. Thermoelectric performance of 2D tellurium with accumulation contacts. *Nano lett.* **19**, 1955–1962 (2019).

98. Guthmann, C. & Thuillier, J. Shubnikov de Haas effect in tellurium. *Solid State Commun.* **6**, 835–838 (1968).

99. Guthmann, C. & Thuillier, J. M. Fermi Surface of Tellurium. *Phys. Status Solidi (b)* **38**, 635–642 (1970).

100. Bresler, M., Farbstein, I., Mashovets, D., Kosichkin, Y. V. & Veselago, V. Experimental determination of the shape of the hole Fermi surface in tellurium. *Phys. Lett. A* **29**, 23–24 (1969).

101. Button, K. J., Landwehr, G., Bradley, C., Grosse, P. & Lax, B. Quantum effects in cyclotron resonance in p-type tellurium. *Phys. Rev. Lett.* **23**, 14 (1969).

102. Anzin, V. et al. Inversion asymmetry splitting of Landau levels in tellurium. *Solid State Commun.* **8**, 1773–1777 (1970).

103. Von Klitzing, K. & Landwehr, G. Surface quantum states in tellurium. *Solid State Commun.* **9**, 2201–2205 (1971).

104. Silbermann, R. & Landwehr, G. Surface quantum oscillations in accumulation and inversion layers on tellurium. *Solid State Commun.* **16**, 1055–1058 (1975).

105. Bouat, J. & Thuillier, J. Surface quantum transport in tellurium inversion layers. *Surf. Sci.* **73**, 528–536 (1978).

106. Qiu, G. et al. Quantum transport and band structure evolution under high magnetic field in few-layer tellurene. *Nano Lett.* **18**, 5760–5767 (2018).

107. Agapito, L. A., Kioussis, N., Goddard, W. A. III & Ong, N. P. Novel family of chiral-based topological insulators: elemental tellurium under strain. *Phys. Rev. Lett.* **110**, 176401 (2013).

108. Hirayama, M., Okugawa, R., Ishibashi, S., Murakami, S. & Miyake, T. Weyl node and spin texture in trigonal tellurium and selenium. *Phys. Rev. Lett.* **114**, 206401 (2015).

109. Ideue, T. et al. Pressure-induced topological phase transition in noncentrosymmetric elemental tellurium. *Proc. Natl Acad. Sci. USA* **116**, 25530–25534 (2019).

110. Akiba, K. et al. Magnetotransport properties of tellurium under extreme conditions. *Phys. Rev. B* **101**, 245111 (2020).

111. Akahama, Y., Kobayashi, M. & Kawamura, H. Pressure-induced superconductivity and phase transition in selenium and tellurium. *Solid State Commun.* **84**, 803–806 (1992).

112. Rodriguez, D. et al. Optical signatures of phase transitions and structural modulation in elemental tellurium under pressure. *Phys. Rev. B* **101**, 174104 (2020).

113. Rodriguez, D. et al. Two linear regimes in optical conductivity of a type-I weyl semimetal: the case of elemental tellurium. *Phys. Rev. Lett.* **124**, 136402 (2020).

114. Nakayama, K. et al. Band splitting and Weyl nodes in trigonal tellurium studied by angle-resolved photoemission spectroscopy and density functional theory. *Phys. Rev. B* **95**, 125204 (2017).

115. Tsirkin, S. S., Puente, P. A. & Souza, I. Gyrotropic effects in trigonal tellurium studied from first principles. *Phys. Rev. B* **97**, 035158 (2018).

116. Chang, G. et al. Topological quantum properties of chiral crystals. *Nat. Mater.* **17**, 978–985 (2018).

117. Zhang, N. et al. Magnetotransport signatures of Weyl physics and discrete scale invariance in the elemental semiconductor tellurium. *Proc. Natl Acad. Sci. USA* **117**, 11337–11343 (2020).

118. Gopalan, V. & Litvin, D. B. Rotation-reversal symmetries in crystals and handed structures. *Nat. Mater.* **10**, 376–381 (2011).

119. Koma, A. & Tanaka, S. Etch pits and crystal structure of tellurium. *Phys. Status Solidi (b)* **40**, 239–248 (1970).

120. Blakemore, J. & Nomura, K. Enantiomorphous character of etch pits in tellurium. *J. Appl. Phys.* **32**, 745–746 (1961).

121. Dong, Z. & Ma, Y. Atomic-level handedness determination of chiral crystals using aberration-corrected scanning transmission electron microscopy. *Nat. Commun.* **11**, 1588 (2020).

122. Yoda, T., Yokoyama, T. & Murakami, S. Current-induced orbital and spin magnetizations in crystals with helical structure. *Sci. Rep.* **5**, 12024 (2015).

123. Furukawa, T., Shimokawa, Y., Kobayashi, K. & Itou, T. Observation of current-induced bulk magnetization in elemental tellurium. *Nat. Commun.* **8**, 954 (2017).

124. Şahin, C., Rou, J., Ma, J. & Pesin, D. Pancharatnam-Berry phase and kinetic magnetoelectric effect in trigonal tellurium. *Phys. Rev. B* **97**, 205206 (2018).

125. Rikken, G. L. J. A. & Avarvari, N. Strong electrical magnetochiral anisotropy in tellurium. *Phys. Rev.* **B99**, 245153 (2019).

ACKNOWLEDGEMENTS

AUTHOR CONTRIBUTIONS

P.D.Y. and G.Q. conceived the outline of the review and structured the paper. G.Q. drafted the "Introduction" and "Conclusion and Outlook" section and prepared the figures. Y.W. and W.W. wrote the section "Routes towards 1D and 2D tellurium". A.C. contributed to the section "Te-based CMOS and advanced device applications". C.N. and G.Q. wrote the section "Novel physical properties in tellurium". G.Q. and P.D.Y. merged all the sections into the manuscript which was polished and proofread by A. C. All authors have discussed the results in the paper and approved the content of the paper.

COMPETING INTERESTS

The authors declare no competing interests.

ADDITIONAL INFORMATION